Received: 15 July 2022 | Revised: 15 September 2022 | Accepted: 4 October 2022

DOI: 10.1002/ppap.202200129

RESEARCH ARTICLE

PLASMA PROCESSES AND POLYMERS

Silicon nanocrystal synthesis with the atmospheric plasma source HelixJet

Maren Dworschak[1] | **Niklas Kohlmann**[2] | **Filip Matějka**[3] | **Pavel Galář**[3] | **Lorenz Kienle**[2] | **Jan Schäfer**[4] | **Jan Benedikt**[1,5]

[1]Group of Experimental Plasma Physics, Institute of Experimental and Applied Physics, Kiel University, Kiel, Germany

[2]Group of Synthesis and Real Structure, Institute of Material Science, Kiel University, Kiel, Germany

[3]Department of Thin Films and Nanostructures, Institute of Physics, Czech Academy of Sciences, Prague, Czech Republic

[4]Division Materials and Surfaces, Leibniz Institute for Plasma Science and Technology, Greifswald, Germany

[5]Kiel Nano, Surface and Interface Science KiNSIS, Kiel University, Kiel, Germany

Correspondence
Maren Dworschak and Jan Benedikt, Institute of Experimental and Applied Physics, Experimental Plasma Physics, Kiel University, Leibnizstr. 19, Kiel 24098, Germany.
Email: dworschak@physik.uni-kiel.de and benedikt@physik.uni-kiel.de

Funding information
Deutsche Forschungsgemeinschaft, Grant/Award Numbers: 426208229, KI 1263/17-1

Abstract

The HelixJet, a plasma source operating under atmospheric pressure with RF power, was used for the synthesis of silicon nanoparticles (Si-NPs) in the context of relevance in nanomedicine, sensor technology, and nanotechnology. The HelixJet was operated with a variety of He/Ar/H_2/SiH_4 gas mixtures to characterize the Si-NPs in regard to their size, crystallinity, structure, and photoluminescence. Distinct varieties of nanomaterials in the size range from 3 nm to over 100 nm were synthesized depending on the operation parameters of the HelixJet. Admixture of H_2 alongside high RF powers led to the formation of crystalline nanoparticles with a strong photoluminescence intensity, where the photoluminescence properties as well as the nanocrystal synthesis yield were tunable by adjustment of the synthesis parameters. Post-synthesis in-flight annealing allowed the formation of large crystalline nanoparticles. In addition, the experiments conducted in this study resulted in a design improvement of the HelixJet plasma source that extends the stability of the operating range. Furthermore, the added spatial separation of the He/H_2 and He/Ar/SiH_4 streams (SiH_4 injection on-axis) minimizes material deposition within the HelixJet and enables continuous long-term operation.

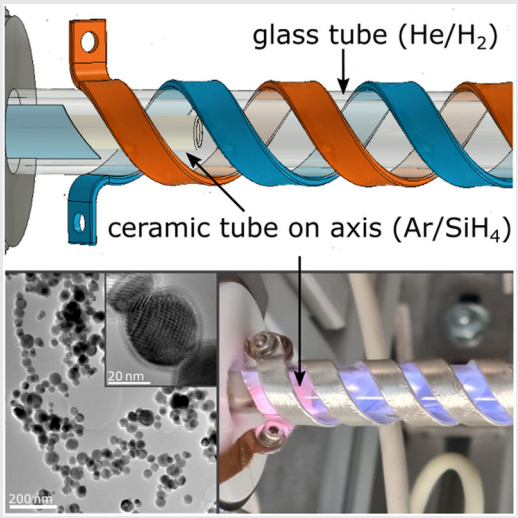

KEYWORDS
atmospheric pressure plasmas, photoluminescence, silane, silicon nanocrystals

1 | INTRODUCTION

Silicon nanoparticles (Si-NPs) represent a class of nanomaterials that are currently being studied very intensively since their application in nanotechnology and in the field of life science opens up surprising possibilities. For example, Fu et al. published the unique optical characteristics of spherical Si-NPs.[1] Depending on the size of the Si-NPs and the wavelength of the incoming light, the Si-NPs exhibit a direction-dependent light scattering. This feature is crucial for the production of new metamaterials and nano-antenna devices. For light-on-chip technology, the production of defined Si-NPs with the required shape and size is absolutely essential. The current technology uses complex vacuum reactors for this.[2] Precise and efficient production of Si-NPs at atmospheric pressure would thus be a breakthrough.

Another use of optically active nanomaterials is their in vivo application for diagnostic and therapeutic purposes. These nanomaterials have to meet many important requirements such as being nontoxic and not triggering undesirable metabolic reactions. They should be broken down systematically in a short time and not accumulate in the body. In this context, Park et al. 2009 published a study that points to the relevance of porous silicon nanoparticles as a drug carrier, which has not yet been explored sufficiently.[3] Their fundamental diagnostic properties are near-IR photoluminescence, which allows monitoring of both their accumulation and degradation in vivo.

Moreover, a special subclass of Si-NPs is silicon nanocrystals (Si-NCs) with diameters below 10 nm. The quantum confinement effects result in a changed band structure and direct band-gap behavior with the band gap being controlled by the nanoparticle size and its passivation. Si-NCs are investigated since the 1990s with increasing interest due to their potential exciting applications in the microelectronic, photonic, photovoltaic, and nanobiotech industries.[4] Low-pressure plasmas have been used as the method of choice for nanocrystal generation due to a very good size control with narrow size distributions and the ability of surface passivation.[5] This is maintained by the nonequilibrium nature of the low-pressure plasmas, where a negative nanoparticle charge prevents their agglomeration and where selective heating due to surface recombination processes promotes particle crystallization even under conditions with low gas temperature.[6]

Atmospheric pressure nonequilibrium plasmas have been investigated as alternative sources for the synthesis of Si-NCs as well.[7–11] The advantages of this technology are the operation without vacuum equipment which opens up modular configuration options in situ or the combination with other systems. In particular, the particle extraction and connection to a scanning mobility particle sizer (SMPS) are very easy and allow for qualitative improvements in technology regarding the control of particle size distribution. However, the disadvantages include low particle yields, low efficiency, clogging of plasma nozzles, and thus limited stability and reproducibility of the process.

The above examples show the urgency of the Si-NP studies with regard to their controlled efficient production resulting in a defined shape, size, and optical activity. For this study, we decided to investigate the synthesis of Si-NPs and Si-NCs by means of a plasma jet introduced by Schäfer et al. in 2020 as the HelixJet, which is operated at atmospheric pressure by RF power.[12] The HelixJet has demonstrated surprising versatility in recent applications due to its unusual properties compared to other plasma nozzles. This is mainly based on the radial homogeneity of its plasma across and along the discharge space, where other sources of atmospheric plasma contract into a filamentary structure. In HelixJet, filaments are not formed, even in a tube with a diameter of 1 cm. In addition, it is a source that is economical in terms of gas consumption. These properties have been advantageously used for the defined treatment of plastic microparticles used for 3D printing or for the synthesis of stoichiometrically pure silica as corrosion protection.[12,13]

2 | EXPERIMENTAL SETUP AND DIAGNOSTICS

2.1 | HelixJet

The so-called HelixJet is a plasma jet with a double-helix electrode configuration (see Figure 1a). The design of the HelixJet was inspired by the investigations on self-organization phenomena in the plasma jet named ntAPPJ.[14] It could be shown previously that filaments tend to self-assemble. They form equidistant groups and, under certain conditions, are able to rotate at high speeds.[15] During filament rotation (locked mode), filaments are twisted spirally while the inclination correlates with the radial velocity. The HelixJet was designed in a way that the electric field lines match the tilt of filaments in the original self-organized jet. Hence, the stable and uniform conditions of the plasma generated by the HelixJet can be explained by the synergy between self-organization mechanisms and the optimal spiral arrangement of the double-helix electrodes. The electrodes are placed around a 22 cm long quartz

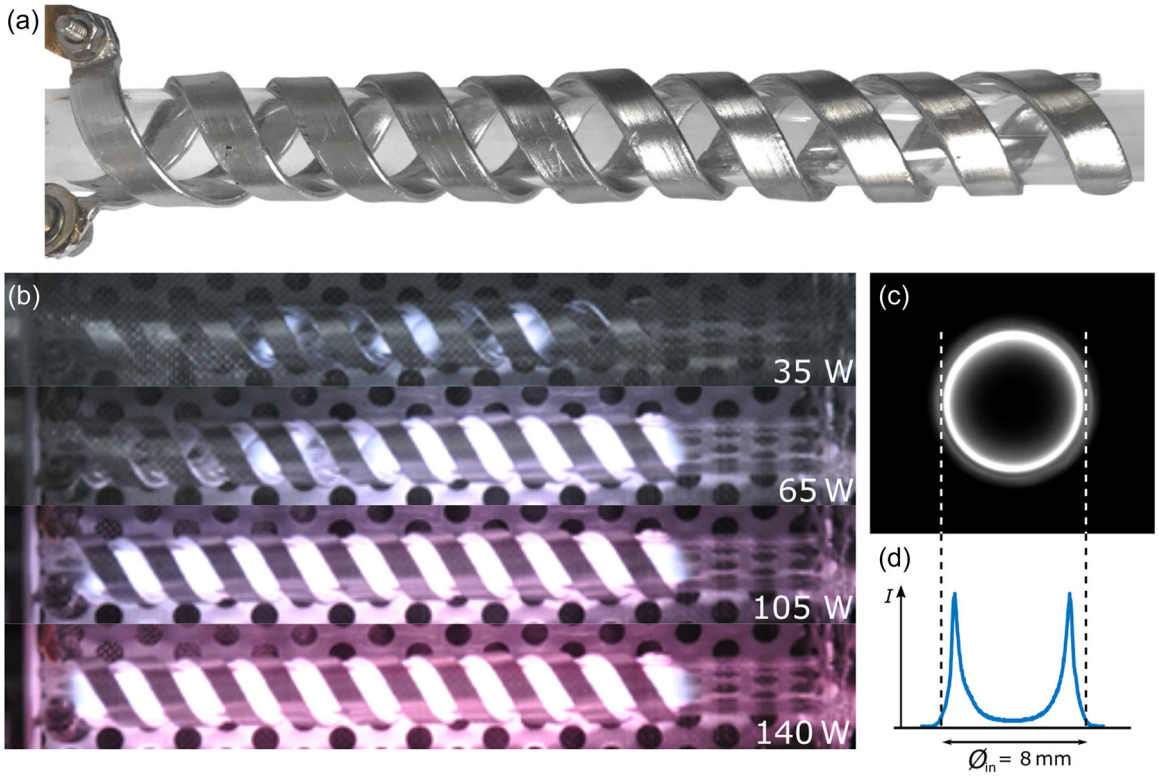

FIGURE 1 Side-view images of the HelixJet without plasma (a) and with a pure helium plasma at various powers (b). Increasing the applied power enables the jet to be operated at its full length. The front view taken with a telecentric lens (c) and the corresponding intensity profile (d) of a plasma emission with 5 ppm silane concentration.

glass tube with an inner diameter of 8mm and a wall thickness of 1 mm. One of the helix electrodes is grounded, while the other one is driven by a 13.56 MHz generator with impedance matching. Powers entering the matchbox are measured with a Z-Scan RF measurement probe (advanced energy). Measured powers range from 20 to 230 W with corresponding peak-to-peak-voltages between 400 and 700 V_{pp}.

In general, the HelixJet can be operated in noble gases with admixtures of molecular gases or particles. Here, the plasma has been generated in helium at flows as low as 100 standard cubic centimeters per minute (sccm) and with small admixtures of SiH_4 as a precursor. During its operation, the jet is always cooled with a constant flow of compressed air to ensure uniform and reproducible behavior. An example of the HelixJet's discharge is shown in Figure 1b. This side view shows how the discharge is able to fill the whole volume in between the electrodes when the power is increased. Figure 1c,d shows a front image taken with a telecentric lens and a Basler acA1440 camera and the corresponding light emission intensity profile at an admixture of 5 ppm, respectively. The radial profile of the emitted radiation shows increased intensity towards the walls of the jet, which is the typical behavior of an atmospheric plasma operated in γ-mode as described in Yang et al.[16] Apart from this, the intensity profile shows spatial homogeneity, which has a significant effect on the efficiency of the process in the tube. The resulting plasma density is expected to be homogeneous across the tube as presented for example in Shi et al.[17] Based on a comparison with the published results in an argon discharge at a time resolution of ns,[12] it can be assumed that even at the conditions here, the discharge is quasi-stationary without any visible modulations.

2.1.1 | HelixJet modifications

The particle yield at atmospheric pressure is low when working with small reactive gas admixtures. For most analytical methods and applications it is crucial to have a sufficient amount of nanoparticles collected in a short time. To achieve this, the admixture of silane has to be increased. However, when the HelixJet is operated with a large admixture of strongly electronegative silane, the discharge becomes unstable. This can be observed over the extension of the discharge which is not filling the whole interelectrode volume anymore and gets shorter (as it is seen for the helium case and low power operation

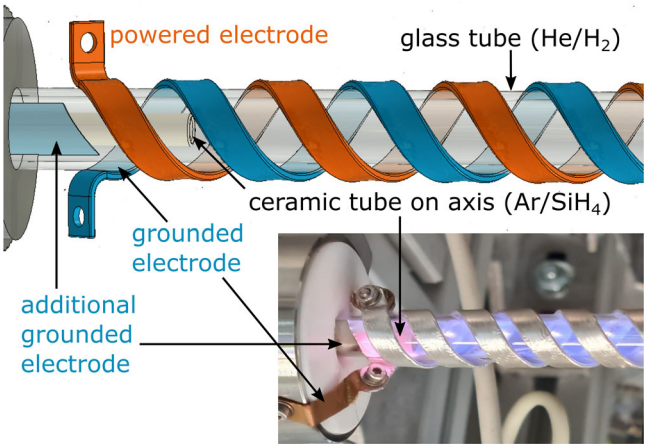

FIGURE 2 CAD-sketch of the modified HelixJet (top) and depiction of the actual experiment (bottom). Additionally to the helix-shaped electrodes, a grounded tantalum electrode (blue) has been inserted into the quartz glass tube. It is placed in close proximity to the driven electrode (red). The gas inlet has been altered to a configuration, where the silane is injected on-axis to reduce deposition on the tube's inner wall.

in Figure 1) or extinguishes completely. This effect can be counteracted by increasing the applied power until the discharge is filling the whole volume again, but this power is limited in our case. Additionally, powers exceeding 230 W have been causing overheating of the electrodes. The original HelixJet setup has been, therefore, modified with an additional electrode inserted into the glass tube and with the on-axis injection of the reactive gas as shown in Figure 2.

The additional grounded electrode is cut at the same angle as the helices and is positioned in close proximity to the driven RF-helix-electrode. With these modifications, a plasma is easily ignited in the large electric field at this additional grounded electrode. The absence of silane in this region (see later) prevents any deposition here. This additional plasma provides ions, electrons, and high-energy photons that facilitate the ignition and operation of the regular plasma inside the HelixJet. Tantalum was chosen as a material for this second electrode due to its lower vapor pressure at elevated temperatures.[18] The second modification is concerning gas injection. With the previous model, all gases (reactive and noble) were premixed and then fed into the plasma. The on-axis gas injection approach splits the gas injection into an outer and inner flow. Noble gases and hydrogen can be fed through the outer flow whereas the silane diluted in noble gas is fed through the ceramic tube on the jet's axis. The ceramic tube has a diameter of 4 mm and a wall thickness of 0.7 mm. This approach limits the contact of the high-density plasma at the quartz glass tube inner wall with silane and thus reduces thin film deposition there. The position of the inner capillary is adjusted in a way that injects the silane downstream of the additional grounded electrode to prevent particle formation or material deposition there. The evidence of the spatially separated gas injections can be seen at the bottom right of Figure 2. The first plasma consisting of only the carrier gas helium is emitting in orange, while the following plasma contains the additional admixture of 0.01% silane diluted in argon and is therefore glowing in the typical violet argon color. These measures result in an even longer lifetime of the HelixJet (half a year and counting) compared to a premixed gas injection (deposition visible after a day) due to further elimination of material deposition inside the jet.

2.2 | SMPS

SMPS can be used to measure size distribution functions from a polydisperse stream of submicrometer particles down to diameters approaching 1 nm. The SMPS used in this paper was a TSI Universal-SMPS (Model 3938). Particles exiting the HelixJet pass through an aerosol neutralizer, where a known charge distribution is established according to Wiedensohler et al.[19] The particles are then fed into the differential mobility analyzer (DMA). In this paper, two different DMAs were used. The 1-nm-DMA (Model 3086) was used for well-resolved classification of particles between 1 and 50 nm. The Long DMA (Model 3081A) was used for particle sizes up to 1000 nm. Both models consist of two aligned cylindrical electrodes with respective radii r_i and r_a and length L. The inner cylinder is charged positively. Only particles of a certain electric mobility μ can pass the DMA and reach its outlet for a set voltage U_{DMA}.

$$U_{\mathrm{DMA}} = \frac{Q \times \ln\left(\frac{r_i}{r_a}\right)}{2\pi L \mu}, \tag{1}$$

where Q describes the gas volume flow. Under the assumption of spherical particles, the particle diameter d and electric mobility μ are correlated by Stokes' Law.

$$\mu = \frac{neC}{3\pi\eta d}, \tag{2}$$

where n is the number of elementary charges on the particle, e the elementary charge, η the dynamic gas viscosity, and C the Cunningham slip correction, which can be found in Kim et al.[20] A condensation particle counter (CPC) can be positioned downstream of the DMA. Particles leaving the DMA pass through a chamber saturated with n-butyl alcohol. The vapor condensates on each particle making them increase in size until they can

be detected by an opacity meter. When working with the SMPS, a transfer function for diffusion losses of particles in the flow path within the SMPS was used, which is especially important when particles below 100 nm are sized. With the setup described, the SMPS is not only limited to measuring particle size distribution functions but it can also be used to select the particle size on demand. By applying a certain voltage U_{DMA}, only particles with a certain diameter (certain mobility) can pass the device and can then be collected behind it. We stress here that this selection of particle size "on demand" can currently be realized with high flexibility and accuracy only with atmospheric plasma sources providing an additional argument for their further development and characterization.

2.3 | Electron microscopy

Direct investigation of particle sizes, crystal structure, and chemical composition was performed by transmission electron microscopy (TEM) as well as scanning electron microscopy (SEM). The TEM used in this paper was an FEI Tecnai F30 G^2 STwin operated at 300 kV. Scanning electron microscopy measurements were conducted on a ZEISS Sigma 300 Field emission SEM operated at 30 kV. TEM samples were either obtained by placing TEM Cu grids with a lacey carbon carrier film (Plano GmbH) below the output of the jet or by gentle pressing of the grid onto a particle-coated Si wafer in the case of fluorescent nanoparticles. The crystallographic phase of the synthesizes material is investigated both by high-resolution TEM (HRTEM) as well as selected area electron diffraction (SAED). TEM energy dispersive X-ray spectroscopy (EDXS) is used to analyze the chemical composition. The Z-contrast of high-angle annular dark field (HAADF) scanning TEM (STEM) is used to identify whether single particles or clusters of particles were synthesized for a given set of parameters.

2.4 | Steady-state and time-resolved photoluminescence spectroscopy

A thorough description of the system for steady-state photoluminescence (PL) spectroscopy as well as the one for time-resolved measurements can be found in Galář et al.[21] In brief, the spectra of the silicon nanocrystals were collected using a Shamrock 300i (Andor, Oxford Instruments) spectrograph coupled with an EMCCD camera (Newton 970, Andor, Oxford Instruments). The nanoparticles were collected on silicon wafers and those samples were excited using a continuous laser beam at 325 nm generated by a HeCd laser. The initial laser intensity (≈2.8 mW) was reduced to ≈0.5 mW by ND filters to eliminate potential surface modification of the nanocrystals. The measurements were realized at ambient conditions and the resulting spectra were corrected to the spectral sensitivity of the whole system. The laser pulses exciting the samples in the time-resolved setup were generated using a laser cascade composed of a femtosecond Pharos SP (light conversion) laser and a HiRo (light conversion) harmonic generator. The original IR pulses (1030 nm, 1 kHz repetition rate) were converted by HiRo into ones of 343 nm. The output pulse intensity was decreased to about 60 μJcm^{-2} which corresponds to about 10^{14} photons per square centimeter. The resulting PL signal was collected using a streak camera (Hamamatsu) coupled with an imaging spectrometer. As a proof of minimal modification of the samples during measurements, the spectra of each sample were collected two times and the data were accepted only in case that both measurements were matching. The data were processed and analyzed using a procedure published in Kůsová and Popelář.[22] Here the influence of a finite pulse duration on the PL decays was eliminated using deconvoluted data. The signal-to-noise ratio was increased by integration over four spectral neighboring decays. The onset was determined using a single exponential fit. Afterward, the decays were fitted precisely by a stretched-exponential function.

$$I = I_0 \cdot \exp\left[-\left(\frac{t}{\tau}\right)^{\beta}\right], \tag{3}$$

where τ is the time constant and β is the stretching exponent. This function describes the superposition of exponential functions which, because of the size distribution of nanocrystals, commonly describes exciton-related PL decays of silicon nanocrystals well.

The final average decay time at a specific wavelength was obtained using:

$$\tau_{av}(\lambda) = \frac{\Gamma\left(\frac{2}{\beta(\lambda)}\right)}{\Gamma\left(\frac{1}{\beta(\lambda)}\right)}\tau(\lambda). \tag{4}$$

3 | RESULTS AND DISCUSSION

3.1 | Standard helix jet

This section covers the results obtained with the unmodified standard HelixJet. It has been operated at an overall flow of 800 to 2000 sccm, which results in a residence time of the particles in the plasma between 200 and 600 ms. The noble carrier gas is helium, and the

reactive gas for particle production is 0.01% silane diluted in argon, meaning that the amount of argon in the gas mixture is changing with the silane admixture. Silane concentrations are given in ppm and hydrogen concentrations in %.

The particle production and particle properties have been studied through various analytical methods. The SMPS has been used to analyze the mean particle diameter of the nanoparticles that are synthesized with the HelixJet at different concentrations of silane (see Figure 3). For a constant overall flow of 1000 sccm, the silane concentration has been adjusted between 1 and 36 ppm for a constant power of 125 W. This has led to the synthesis of nanoparticles in the range of 10 nm up to 100 nm. To synthesize nanoparticles below 10 nm, the gas flow of the carrier gas helium was increased at a constant flow of silane. This reduced the particle diameter as seen in the inset in Figure 3.

The nanoparticles synthesized in the HelixJet have been analyzed with SEM measurements. To decrease the amount of collected particles for microscopy methods, one particle diameter is selected from the distribution function using the DMA voltage. The particles have been collected on a holey carbon TEM grid. It is found, that for increased silane concentrations, smaller nanoparticles agglomerate to bigger ones and are detected by the SMPS as such. Here, only an effective aerodynamic diameter of the agglomerate is measured by the SMPS based on the drift properties of the agglomerate. This is demonstrated in Figure 4, where preselecting nanoparticles with a diameter of 50 nm in the SMPS (remember they are assumed to be spherical particles to calculate

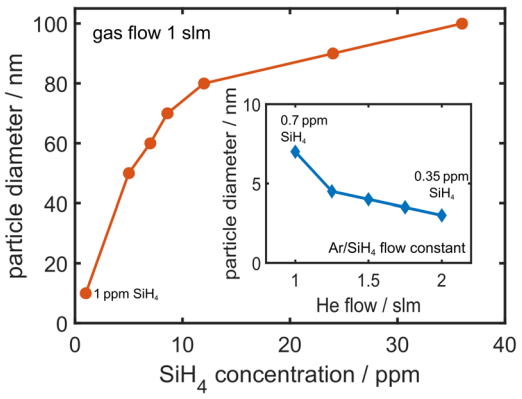

FIGURE 3 Dependence of mean particle diameter on silane concentration as measured with SMPS for the total gas flow of 1000 sccm and a power of 125 W. Inset: Dependence of mean particle diameter on helium flow. Increasing the helium flow decreases the SiH_4 concentration while the Ar/SiH_4 flow is constant during the measurements.

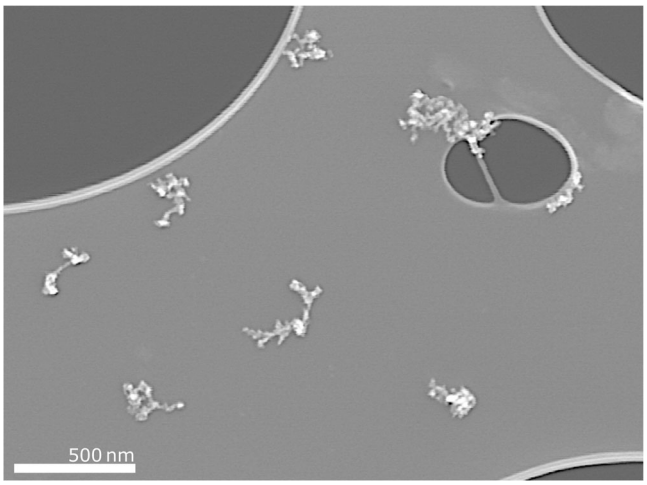

FIGURE 4 SEM image of amorphous silicon nanoparticle agglomerates generated at 33 ppm silane admixture and 125 W collected on a holey carbon TEM grid. The particle diameter was pre-selected by the SMPS to be 50 nm. SEM, scanning electron microscopy.

their mobility) resulted in agglomerates composed of several tens of roughly 10 nm large particles.

3.1.1 | Annealing stage results

By introducing an annealing stage in the form of a muffle furnace, the initially synthesized agglomerates (as shown in Figure 4) could be fused into smaller crystalline particles with the measured mean diameters corresponding to the real diameter. To achieve this, the particles are led through the furnace (1100°C) in stainless steel tubing. The path through the oven is 2 m long which results in a "time of flight" of around 9 s in the oven. Figure 5 shows four different size distribution functions that have been measured with the SMPS. The dashed lines belong to a SiH_4 concentration of 13 ppm. At room temperature (blue) this concentration produces particles with an effective measured mean diameter 10 nm. After being treated in the annealing stage, the mean diameter reduces to 6 nm as it can be seen in the red curve. An even more significant change in diameters through the introduction of the annealing stage is observed for an increased concentration of 36 ppm (solid lines). Here the mean particle diameter decreases from 90 nm mean diameter at room temperature (blue) to 40 nm mean diameter (red) after passing the annealing stage. The resulting particles of this adapted synthesis process have the real size corresponding to their aerodynamic size as seen in Figure 6a and are fully crystalline with a thin amorphous shell as seen from HRTEM in the inset of the same figure.

These annealed nanoparticles are fully crystalline, yet often consist of multiple crystallites as seen from the moiré pattern in Figure 6a. The nanoparticles synthesized in this manner have relatively wide size distributions up to 100 nm in diameter and even monocrystalline particles with diameters up to 200 nm could be found. Elemental analysis via EDXS revealed a stoichiometry of 41 atm% Si, 29 atm% Mn, and 26 atm% O. Traces of Cr could be detected as well. Due to the close proximity of the Mn-L and O-K lines, it is likely, that the amount of oxygen is overestimated in the EDXS quantification. A non-negligible amount of manganese alongside traces of chromium is a consequence of the manganese and chromium in the stainless steel alloy of the tubing in the annealing stage. Manganese has a relatively high vapor pressure compared to other metals, so it is released from the metal earlier than other components of the alloy. Together with the high annealing temperatures exceeding 1000°C it is present in the annealing stage and gets incorporated into the particles. Using another alloy can lead to the formation of different silicides or ceramic/glass tubing could be used to avoid silicide formation at all.

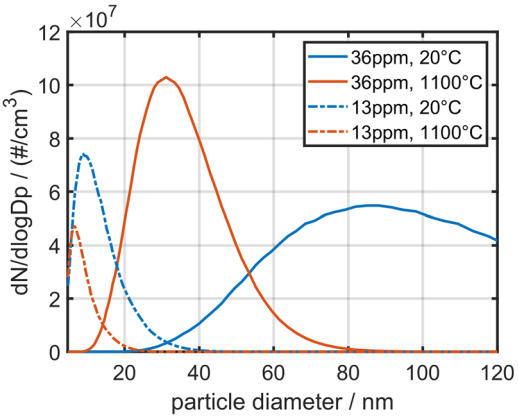

FIGURE 5 Size distribution functions for two different silane concentrations. Each measured after the annealing stage first at room temperature 20°C and second at 1100°C. Total gas flow 800 sccm.

Analysis of the crystallographic phase of the particles via electron diffraction reveals that Mn_4Si_7, as well as MnSi, are the dominant phases, (see Figure 6b). Distinct reflections originating from each phase only show that particles of both phases are synthesized simultaneously. A small amount of crystalline Si material is present as well, as indicated by the weak 111 reflection of Si. Particles of both phases have been identified from HRTEM and fast Fourier transform (FFT) analysis. Looking at the overall stoichiometry determined via EDXS a phase mixture of Mn_4Si_7 and MnSi is in good agreement with the ratio of Mn to Si obtained from EDXS quantification. The particles are stable in air and no effects of oxidation have been observed when investigating samples again several weeks after their synthesis even after having been stored in ambient conditions for a prolonged time. HRTEM shows an amorphous layer around the particles (Figure 6a). It is likely that this layer is made up of silicon and/or manganese oxide and it prevents further oxidation of the particle cores. The short time of flight of roughly 9 s (see Section 3.1.1) is highly likely not sufficient for the crystallites in the particles to

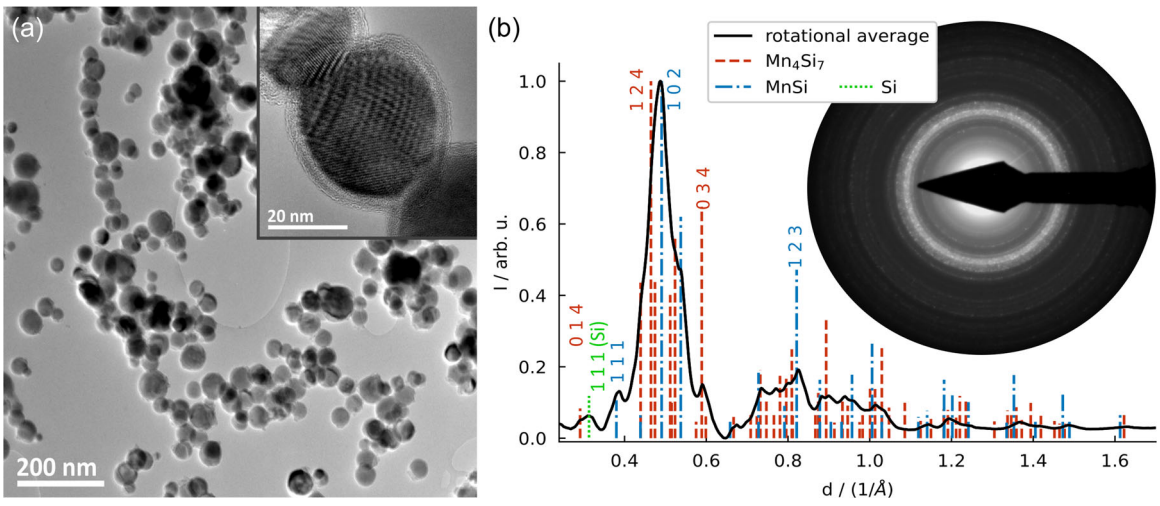

FIGURE 6 TEM micrograph (a) of crystalline nanoparticles of various sizes synthesized with identical plasma parameters as in Figure 4 with the addition of an annealing stage at 1100°C with the inset showing an HRTEM micrograph of a 20 nm particle. (b) SAED pattern and the corresponding rotational average of a large number of the particles shown in (a). Rotational average shows that MnSi alloys are dominant. SAED, selected area electron diffraction; TEM, transmission electron microscopy.

fully merge. Introducing a longer tubing, and thus a longer annealing time could enable the synthesis of single-crystalline particles in the future.

Higher manganese silicides (HMS) such as Mn_4Si_7, Mn_7Si_{12}, $Mn_{11}Si_{19}$, and so on have a direct band gap of about 0.7 eV and show ferromagnetic behavior, which makes them ideal ferromagnetic semiconductors for optoelectronic applications. Mn_4Si_7 and other HMS compounds have been studied for example in Liu et al.[23] Possible other applications for crystalline silicon particles on the larger end of the size scale include all-dielectric nanophotonics.[24] Also, quantum emitters could be coupled to these silicon nanospheres instead of being coupled to plasmonic (metallic) nanoparticles. This would result in various advantages, since metals can normally lead to nonradiative resonances and eventually quenching, in contrast to dielectric nanoparticles that could enhance the (spontaneous) emission.[25] Additionally, arrays of these nanoparticles can have photo-crystal or wave-guiding functionalities.[26,27]

3.1.2 | Stability diagram

If the particles are not annealed in an oven, crystallinity can also be achieved by introducing H_2 to the gas mixture. Admixing hydrogen enhances the particle temperature due to selective heating and suppresses oxidation due to the presence of a small amount of gas impurities (mainly H_2O) in the used gas mixture.[6] Additionally, hydrogen-related radicals and ions result in nanoparticle etching, reducing their size. But an increased hydrogen concentration brings the operation of the HelixJet to its limits: Due to the higher ionization energy of hydrogen and much larger concentration of molecular gas in the mixture, a larger power is needed to ignite and sustain the discharge. Figure 7 displays the power P_f that is needed to sustain the discharge at the whole interelectrode volume inside the HelixJet (called the full discharge further on) at different concentrations of reactive gases. It can be seen for the unmodified HelixJet that the power needed for a stable full discharge operation increases with increasing silane concentration. Without hydrogen admixture, up to 160 W is needed to generate the full discharge at the highest silane concentration used. Adding hydrogen, P_f further increases to values of up to 200 W even for small concentrations of silane. The jet can not be safely operated with hydrogen at silane concentrations above 15 ppm. These instabilities result in limited flexibility since small changes in gas composition or other plasma parameters can lead to unstable plasma. Running the jet at these high powers would also result in the heating of

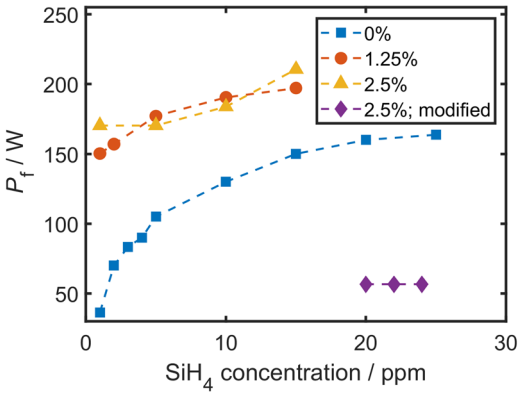

FIGURE 7 Stability diagram showing the minimal power P_f that is needed to ignite the full discharge dependent on the different concentrations of silane. This is shown for different H_2 concentrations and for the modified version of the HelixJet.

all jet components including the generator and matchbox. When collecting particles, the jet has to be operated for a prolonged time and an elevated temperature of those components (which can not be compensated by simple air cooling anymore) can potentially reduce their reliability.

3.2 | Modified HelixJet

Modifications of the original HelixJet have been, therefore, introduced to improve the stability and range of its operation. The purple rhombus symbols in Figure 7 demonstrate, that the jet can now be operated stably at high hydrogen and silane concentrations while only using one-fourth of the power (55 W). The particle production with the modified version of the jet and their properties can be discussed now.

3.3 | SMPS results

3.3.1 | H_2 Admixture

Figure 8 shows the dependency of the effective mean particle diameter as determined with SMPS for different concentrations of hydrogen and silane at a fixed power of 145 W. When using no hydrogen (blue triangles) the particle size increases steeply until a concentration of 5 ppm followed up by a slower linear increase with increasing silane concentration. With this, a particle size of 80 nm can be achieved for a concentration of 25 ppm. Again, it is not expected to be the size of a single particle, but rather an effective diameter of an agglomerate of smaller particles as discussed above for the case of the

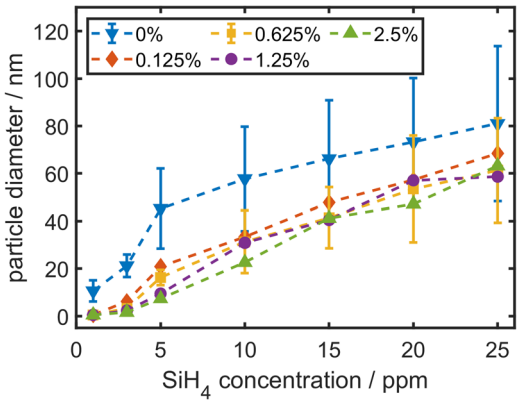

FIGURE 8 Particle mean diameter as measured with SMPS for different concentrations of silane and hydrogen at a fixed power of 145 W and an overall flow of 800 sccm.

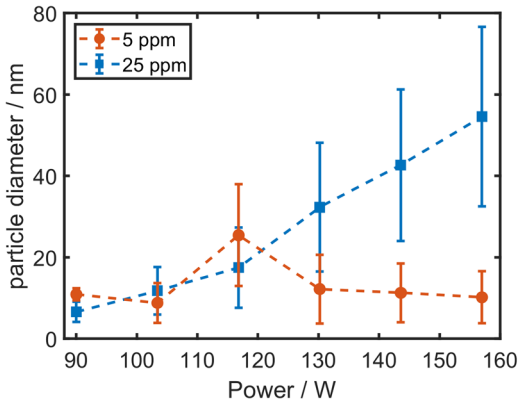

FIGURE 9 Particle or particle agglomerate effective diameter for different applied powers at an overall flow of 800 sccm. Two concentrations of silane were used (5 and 25 ppm). The hydrogen concentration was 1.25% for both.

standard HelixJet. Error bars have been determined from the FWHM of the fitted lognormal distribution of the size distribution function. For a better overview, only error bars for 0% and 1.25% hydrogen admixture are shown. The error bars of all curves with hydrogen are similar.

When adding hydrogen to the gas mixture, the effective mean particle size decreases. This is due to the interaction of atomic and molecular hydrogen with the particles leading to their partial etching as has been observed for silicon films in Nguyen et al.[28,29] Additionally, the presence of hydrogen will contribute to the reduction of oxygen from the surface and hence compensate for the effect of impurities (O_2, H_2O) in the gas mixture. The enhanced selective heating, oxygen removal and hydrogen passivation of defects will improve the nanoparticle properties with respect to crystallinity and stability against post-oxidation. Overall the reduction of the effective diameter of the particle agglomerates is only weakly dependent on the H_2 concentration within the used range of 0.125%–2.5%.

3.3.2 | Effect of power

Figure 9 shows the dependency of the particle diameter for different applied powers P. The experiment was done for two different silane concentrations of 5 and 25 ppm and a hydrogen concentration of 1.25%. The particle size for the smaller silane concentration (red circles) does not change with power, except for one outlier. For a higher concentration, the particle size increases steadily with increasing applied power. Samples synthesized at 90 and 160 W have been investigated via HAADF-STEM to calibrate the particle sizes obtained via SMPS to a direct measurement of the Feret diameter (90 W case) as well as to corroborate our assumption about the formation of particle agglomerates (160W case). Single particles with a diameter of roughly 10nm as well as agglomerates of a few 10 nm particles are observed (see Figure 10a) at an applied power of 90 W. When the power is increased to 160 W larger agglomerates with encircling diameters of 50–100 nm are clearly evident (Figure 10b). HRTEM, as given in Figure 10c), shows that in the case of agglomeration at 160 W individual particles have diameters of less than 10 nm and are amorphous. SAED patterns of the same particles confirm their amorphous nature. At lower silane concentrations, agglomeration of the 10-nm particles does not seem to be happening. At a concentration of 25 ppm single particles still possess diameters of 10 nm or less, yet form increasingly bigger agglomerates when a higher power is applied. The changed value of the available power per silane molecule ratio can provide a plausible explanation for this behavior. All silane molecules are most likely consumed in the particle formation under conditions with 5 ppm of silane. Increasing the plasma density by increasing the applied power does not increase the available amount of precursors, therefore, the amount of generated particles. This seems not to be the case for large silane concentrations of 25 ppm, where an increase of the applied power results in generation of more particles and, consequently, their faster agglomeration. It remains an open question, whether the agglomeration takes place in the plasma or during the transport (≈17 s) from the plasma to the SMPS device. The particles were deposited directly onto carbon film TEM grids, thus, additional agglomeration from sample transfer is minimized. However, it is still likely that some of the larger agglomerates with encircling diameters exceeding the SMPS measurement range have formed during the deposition process. The TEM measurements show, that SMPS analysis provides precise, well-tailored particle diameters in the range of 10 nm and below. When measuring larger nanoparticles under our conditions, it is

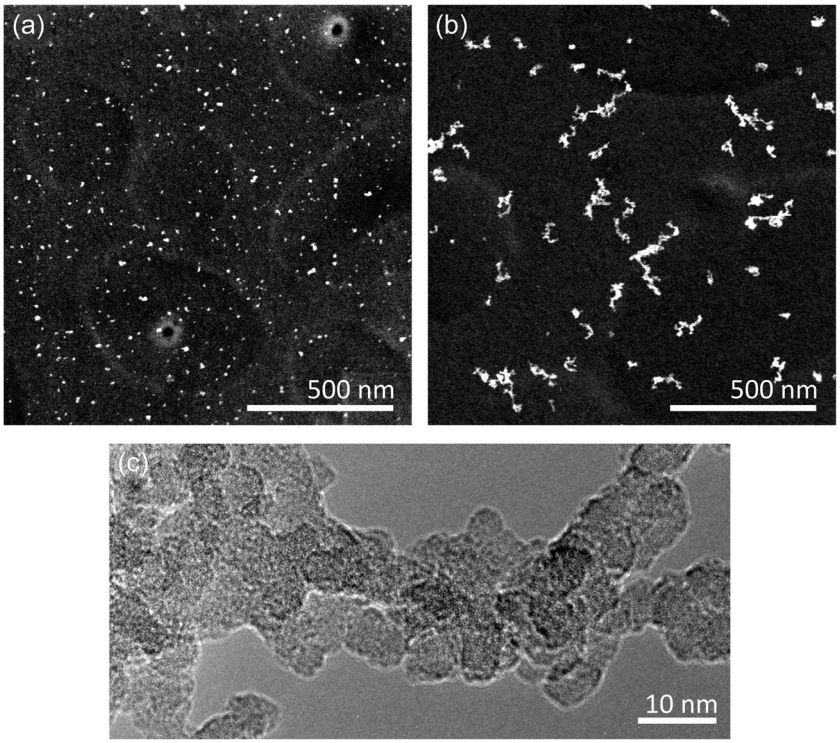

FIGURE 10 HAADF-STEM micrographs of samples created with 25ppm silane concentration at 90W (a) and 160W (b). At higher powers, particles form larger agglomerates as evidenced by HRTEM given in (c). HAADF, high-angle annular dark field; HRTEM, high-resolution TEM; STEM, scanning TEM.

necessary to crosscheck for agglomeration with suitable microscopy methods, whether single spherical particles or particle agglomerates are being measured.

3.4 | Generation of photoluminescent nanocrystals

To test the ability of the modified HelixJet to synthesize silicon nanocrystals, we have produced samples at various experimental conditions. Synthesis conditions varied in the concentration of reactive gases as well as the power of the HelixJet. The samples have been collected on silicon wafers and were analyzed with photoluminescence measurements.

Our studies showed that a strong photoluminescence signal could be achieved for low silane admixtures (5 ppm) and high powers (above 140 W). Hydrogen had to be admixed.

As an example, we present a sample in Figure 11 that has been synthesized with 5 ppm of silane and 0.625% of hydrogen admixture at a power of 145 W.

To elucidate the origin of the photoluminescence of nanocrystals, this sample was further investigated with time-resolved photoluminescence spectroscopy using a streak camera system. In the case of Si-NCs, the photoluminescence can either occur on the surface (charge recombination on traps/functionalization) or in the core of a particle (exciton radiative recombination).[30,31] While surface-related

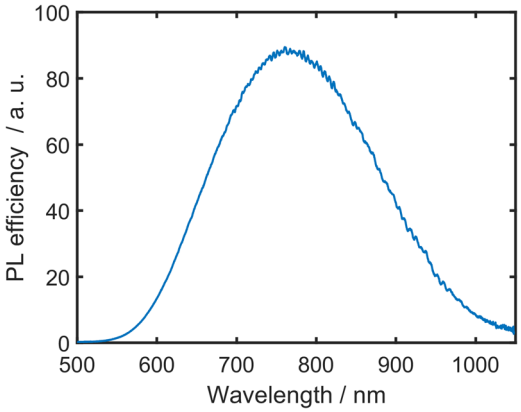

FIGURE 11 Spectral dependence of photoluminescence of a sample created at with admixtures of 5 ppm silane and 0.625% hydrogen at a power of 145 W.

recombination can be manifested in many various ways, the latter results in a multi-exponential/stretch-exponential PL decay at a microsecond timescale.[32] The PL temporal decay of this sample at 700 nm is shown in Figure 12. The PL was excited using laser pulses at 325 nm and an excitation intensity of 80 μJcm^{-2}. Clearly, the decay was multi-exponential showing the average temporal constant of 84 μs. This temporal constant and decay behavior is a sign of well-ordered silicon nanocrystals and corresponds to silicon nanocrystals with homogeneous surface oxygen termination.[33,34]

Particle diameters of this sample can be estimated according to Wen et al.[35] and Mazzaro et al.[32] to be between 3 and 6 nm. To investigate the validity of the size estimations, the nanocrystal sizes, their crystallinity as well as the overall morphology, TEM measurements have been carried out (Figure 13). Figure 13a shows an HRTEM micrograph of our exemplary sample, which was generated with 5 ppm silane and 0.625% H_2. Nanocrystals (identified by visible lattice fringes) alongside amorphous material can be seen. The nanocrystals are clustered together and often embedded in an amorphous phase. Depending on the synthesis parameters, either clustered, single particles or particles completely embedded in an amorphous phase are observed for photoluminescent active samples. For all synthesis parameters, if nanocrystals are formed, they have individual diameters between 5 and 10 nm. To investigate the crystallographic phase of the nanocrystals SAED is utilized. By using SAED a large number of particles is evaluated, and thus, more representative results are obtained.

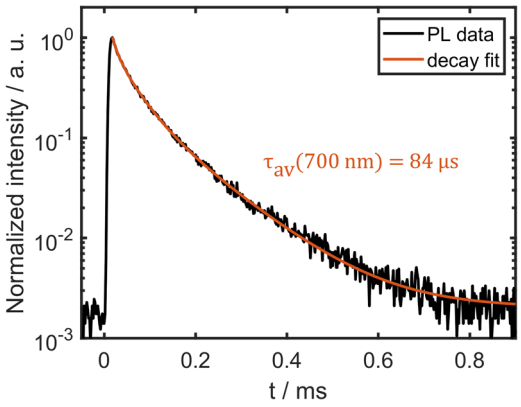

FIGURE 12 Temporal decay of photoluminescence of the exemplary sample (5 ppm silane and 0.625% hydrogen admixture at 145 W) measured at 700 nm. The decay was fitted using a multi-exponential curve, the final average time of the decay was calculated using Equation (3).

The SAED pattern shown in Figure 13b is characteristic of nanocrystalline samples. Due to the presence of larger quantities of amorphous material a strong background intensity is present. For an evaluation, the rotational average is taken and a background subtraction using a fifth-order polynomial background model is applied. The results are in very good agreement with a cubic silicon reference (Figure 13b) clearly proofing the synthesis of Si nanocrystals. EDXS measurements show a stoichiometry of 58 atm% silicon to 42 atm% oxygen. This is consistent with nanocrystals embedded in amorphous SiO_x. Synthesis parameters of 5 ppm silane and 0.625% H_2 thus lead to a large volume fraction of crystalline Si nanoparticles passivated by SiO_x material. The high PL intensity found for these synthesis parameters again confirms the hypothesis that PL intensity scales both with the total amount of active material as well as the volume fraction of nanocrystals to amorphous material. The synthesized nanocrystal-amorphous material system is invariant to oxidation due to storage at ambient conditions. Both the PL intensity as well as the structure as investigated by TEM did not change several months after the initial synthesis. This again is in support of the proposed structure of nanocrystals passivated by SiO_x layers which protects them from further oxidation and provides the surface termination.

Several additional tested conditions typically with high silane concentrations of 25 ppm and low applied

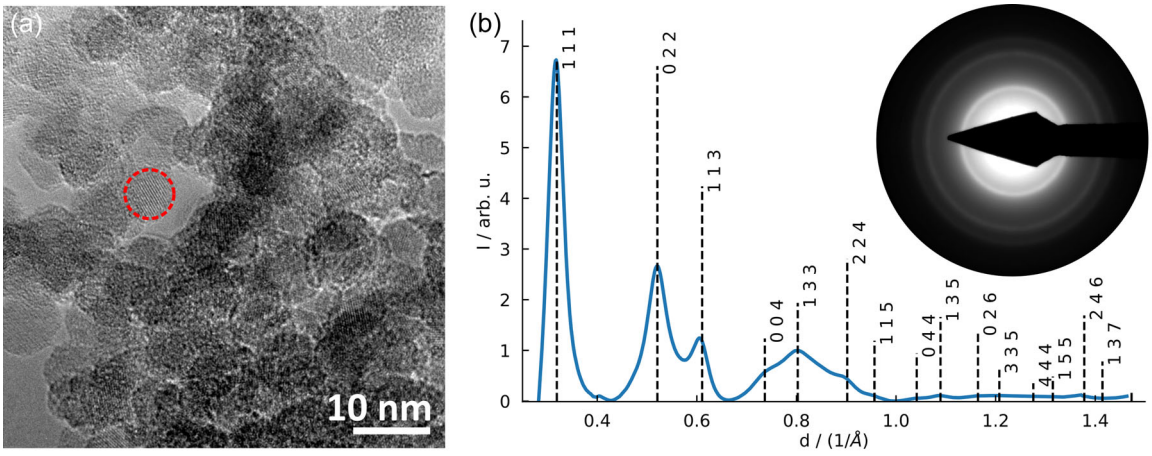

FIGURE 13 (a) HRTEM micrograph of Si nanoparticles synthesized with 5 ppm silane and 0.625% H_2 at 145 W. A crystalline particle with a radius of 7 nm is highlighted. (b) SAED pattern and corresponding rotational average, with calculated reflections from cubic silicon as a reference. HRTEM, high-resolution TEM; SAED, selected area electron diffraction.

powers below 110 W have led to the synthesis of amorphous particles or particle agglomerates without a measurable PL. For these silane admixtures, the maximum particle generation rate can be estimated for an overall flow of 800 sccm to be around 0.3 mg/h. While this exceeds the deposition rate of comparable atmospheric plasma sources, it can still not compete with the generation rates of low-pressure systems that can exceed 100 mg/h.[36]

4 | CONCLUSIONS

The HelixJet has been used successfully to generate a wide range of nanoparticles depending on the synthesis parameters and the use of an annealing stage. Distinct species of nanoparticles could be created: amorphous SiO_x particles, crystalline MnSi nanoparticles, and Si nanocrystals embedded in SiO_x. The stability of the discharge has been increased with modifications in form of an additional electrode and on-axis injection of the SiH_4 molecules allowing the HelixJet to be operated at large admixtures of reactive gases for prolonged times (weeks of continuous operation). The measurements with SMPS, TEM, and the nanoparticle PL have revealed that hydrogen admixture and high applied power lead to the generation of crystalline particles. The combination of silane and hydrogen concentrations can be used to tune the particle size between 3 and 10 nm, where even smaller particles can be probably generated with a further reduction of the silane concentration. The crystalline particles are covered by an amorphous SiO_x layer and show strong photoluminescence nonetheless with a decay time in the range of tens of microseconds. Up to 50 µg/h of SiNCs can be synthesized under the conditions leading to material with a high PL yield (5 ppm silane, hydrogen admixture, powers above 140 W).

High SiH_4 concentrations lead to the formation of larger agglomerates of amorphous ~10 nm diameter nanoparticles. An additional annealing stage can be used to transform these agglomerates into crystalline alloy nanoparticles with broad size distributions and diameters up to 200 nm. SMPS can be used as a filter to collect only particles with the desired size at the differential mobility analyzer with fixed settings. Manganese atoms, originating in the stainless steel tubing used in the annealing stage, have been detected in large amounts in the annealed crystalline particles with MnSi and Mn_4Si_7 being the dominant phases. Using ceramic tubing would avoid metal silicide formation. On the other hand, it suggests a possible synthesis method for these crystals for example for optoelectronic applications.

Overall, this article has demonstrated that the large plasma cross-section, large stability at high admixtures of precursor gases, long operation time, and the ability to tune the nanoparticle properties make the HelixJet a promising atmospheric plasma source for the generation of silicon and other material nanoparticles or nanocrystals.

ACKNOWLEDGMENTS

We gratefully acknowledge funding of this project by the German Research Foundation (DFG, project number 426208229 & KI 1263/17-1) and the Meta-ZIK project "PlasMark" sponsored by the German Federal Ministry of Education and Research (BMBF), grant number 03Z22D511. The German Academic Exchange Service (DAAD) is also acknowledged for the support of researcher exchange between the research groups in Kiel and Prague (project number 57449433). We thank Paul Bittorf for conducting the SEM measurement and Robert Petersen for the photos of the HelixJet. Open Access funding enabled and organized by Projekt DEAL.

DATA AVAILABILITY STATEMENT

The data that support the findings of this study are available from the corresponding author upon reasonable request.

ORCID

Maren Dworschak http://orcid.org/0000-0001-9787-502X
Jan Schäfer http://orcid.org/0000-0002-0652-5057
Jan Benedikt http://orcid.org/0000-0002-8954-1908

REFERENCES

[1] Y. H. Fu, A. I. Kuznetsov, A. E. Miroshnichenko, Y. F. Yu, *Nat. Commun.* **2013**, *4*, 2041. https://doi.org/10.1038/ncomms2538
[2] A. Bapat, C. R. Perrey, S. A. Campbell, C. BarryCarter, U. Kortshagen, *J. Appl. Phys.* **2003**, *94*, 1969. https://doi.org/10.1063/1.1586957
[3] J. H. Park, L. Gu, G. vonMaltzahn, E. Ruoslahti, S. N. Bhatia, M. J. Sailor, *Nat. Mater.* **2009**, *8*, 476. https://doi.org/10.1038/nmat2398
[4] L. Pavesi, R. Turan, *Silicon Nanocrystals Fundamentals, Synthesis and Applications*, Wiley-VCH Verlag, GmbH & Co. KGaA, Weinheim, Germany **2010**.
[5] L. Mangolini, D. Jurbergs, E Rogojina, U. Kortshagen, *J. Lumin.* **2006**, *121*, 327. https://doi.org/10.1016/j.jlumin.2006.08.068
[6] L. Mangolini, U. Kortshagen, *Phys. Rev. E* **2009**, *79*, 1. https://doi.org/10.1103/PhysRevE.79.026405
[7] S. Askari, I. Levchenko, K. Ostrikov, P. Maguire, D. Mariotti, *Appl. Phys. Lett.* **2014**, *104*. https://doi.org/10.1063/1.4872254

[8] T. Nozaki, K. Sasaki, T. Ogino, D. Asahi, K. Okazaki, *Nanotechnology* **2007**, *18*, 235603. https://doi.org/10.1088/0957-4484/18/23/235603
[9] R. M. Sankaran, D. Holunga, R. C. Flagan, K. P. Giapis, *Nano Lett.* **2005**, *5*, 537. https://doi.org/10.1021/nl0480060
[10] B. Barwe, F. Riedel, O. E. Cibulka, I. Pelant, J. Benedikt, *J. Phys. D: Appl. Phys.* **2015**, *48*, 314001. https://doi.org/10.1088/0022-3727/48/31/314001
[11] B. Barwe, A. Stein, O. E. Cibulka, I. Pelant, J. Ghanbaja, T. Belmonte, J. Benedikt, *Plasma Process. Polym.* **2015**, *12*, 132. https://doi.org/10.1002/ppap.201400047
[12] J. Schäfer, A. Quade, K. J. Abrams, F. Sigeneger, M. M. Becker, C. Majewski, C. Rodenburg, *Plasma Process. Polym.* **2020**, *17*, 1900099. https://doi.org/10.1002/ppap.201900099
[13] L. Rebohle, A. Quade, T. Schumann, D. Blaschke, R. Hübner, R. Heller, R. Foest, J. Schäfer, W. Skorupa, *Thin Solid Films* **2022**, *753*, 139257. https://doi.org/10.1016/j.tsf.2022.139257
[14] J. Schäfer, F. Sigeneger, J. Špatenka, C. Rodenburg, R. Foest, *Plasma Phys. Control. Fusion* **2018**, *60*, 014038. https://doi.org/10.1088/1361-6587/aa8f14
[15] J. Schäfer, R. Foest, A. Ohl, K. D. Weltmann, *Plasma Phys. Control. Fusion* **2009**, *51*, 124045. https://doi.org/10.1088/0741-3335/51/12/124045
[16] X. Yang, M. Moravej, G. R. Nowling, S. E. Babayan, J. Panelon, J. P. Chang, R. F. Hicks, *Plasma Sources Sci. Technol.* **2005**, *14*, 314. https://doi.org/10.1088/0963-0252/14/2/013
[17] J. J. Shi, M. G. Kong, *J. Appl. Phys.* **2005**, *97*, 023306. https://doi.org/10.1063/1.1834978
[18] R. Honig, David Sarnoff Research Center, *Vapor Pressure Data for the More Common Elements*, R. C. of America RCA Laboratories Division **1957**.
[19] A. Wiedensohler, H. Fissan, *J. Aerosol Sci.* **1988**, *19*, 867. https://doi.org/10.1016/0021-8502(88)90054-7
[20] J. Kim, G. Mulholland, S. Kukuck, D. Pui, *J. Res. Natl. Inst. Stand. Technol.* **2005**, *110*, 31. https://doi.org/10.6028/jres.110.005
[21] P. Galář, J. Khun, A. Fučíková, K. Dohnalová, T. Popelář, I. Matulková, J. Valenta, V. Scholtz, K. Kůsová, *Green Chem.* **2021**, *23*(2), 898. https://doi.org/10.1039/D0GC02619K
[22] K. Kůsová, T. Popelář, *J. Appl. Phys.* **2019**, *125*, 193103. https://doi.org/10.1063/1.5097065
[23] H. Liu, G. She, X. Huang, X. Qi, L. Mu, X. Meng, W. Shi, *J. Phys. Chem. C* **2013**, *117*, 2377. https://doi.org/10.1021/jp310700r
[24] K. V. Baryshnikova, D. A. Smirnova, B. S. Luk'yanchuk, Y. S. Kivshar, *Advanced Optical Materials* **2019**, *7*(14), 1801350. https://doi.org/10.1002/adom.201801350
[25] Q. Zhao, Z. J. Yang, J. He, *Photon. Res.* **2019**, *7*, 1142. https://doi.org/10.1364/PRJ.7.001142
[26] G. W. Castellanos, S. Murai, T. Raziman, S. Wang, M. Ramezani, A. G. Curto, J. GómezRivas, *ACS Photonics* **2020**, *7*(5), 1226.
[27] S. Murai, G. W. Castellanos, T. V. Raziman, A. G. Curto, J. G. Rivas, *Adv. Opt. Mater.* **2020**, *8*, 1902024. https://doi.org/10.1002/adom.201902024
[28] H. V. Nguyen, I. An, R. W. Collins, Y. Lu, M. Wakagi, C. R. Wronski, *Appl. Phys. Lett.* **1994**, *65*, 3335. https://doi.org/10.1063/1.113024
[29] C. Tsai, G. Anderson, R. Thompson, *J. Non-Crystalline Solids* **1991**, *137-138*, 673. https://doi.org/10.1016/S0022-3093(05)80210-8
[30] D. C. Hannah, J. Yang, P. Podsiadlo, M. K. Chan, A. Demortière, D. J. Gosztola, V. B. Prakapenka, G. C. Schatz, G. C. Kortshagen, R. D. Schaller, *Nano Lett.* **2012**, *12*, 4200. https://doi.org/10.1021/nl301787g
[31] K. Kůsová, L. Ondič, E. Klimešová, K. Herynková, I. Pelant, S. Daniš, J. Valenta, M. Gallart, M. Ziegler, B. Hönerlage, P. Gilliot, *Appl. Phys. Lett.* **2012**, *101*, 143101. https://doi.org/10.1063/1.4756696
[32] R. Mazzaro, F. Romano, P. Ceroni, *Phys. Chem. Chem. Phys.* **2017**, *19*(39), 26507. https://doi.org/10.1039/C7CP05208A
[33] K. Kůsová, *Phys. Status Solidi (A)* **2018**, *215*, 1700718. https://doi.org/10.1002/pssa.201700718
[34] S. Miura, T. Nakamura, M. Fujii, M. Inui, S. Hayashi, *Phys. Rev. B* **2006**, *73*(24), 245333. https://doi.org/10.1103/PhysRevB.73.245333
[35] X. Wen, P. Zhang, T. Smith, R. Anthony, U. Kortshagen, *Sci. Rep.* **2015**, *5*, 22. https://doi.org/10.1038/srep12469
[36] O. Yasar-Inceoglu, T. Lopez, E. Farshihagro, L. Mangolini, *Nanotechnology* **2012**, *23*, 255604. https://doi.org/10.1088/0957-4484/23/25/255604

How to cite this article: M. Dworschak, N. Kohlmann, F. Matějka, P. Galář, L. Kienle, J. Schäfer, J. Benedikt, *Plasma Processes Polym*. **2023**;20: e2200129. https://doi.org/10.1002/ppap.202200129